RESEARCH ARTICLE

A Near-Zero Energy Smart Greenhouse Integrated Into a Microgrid for Sustainable Energy and Microclimate Management

TUAN MINH TRAN, (Member, IEEE), **AHMED OUAMMI**,
AND LOUIS A-DESSAINT, (Life Fellow, IEEE)
Department of Electrical Engineering, École de Technology Supérieure (ETS), Montreal, QC H3C 1K3, Canada
Corresponding author: Tuan Minh Tran (tuan-minh.tran.1@ensmtl.ca)

ABSTRACT This paper presents a novel smart greenhouse integrated into a microgrid (SGIM) designed to optimize energy and microclimate management for sustainable agriculture. The SGIM integrates photovoltaic (PV) panels, a micro-combined heat and power (micro-CHP) unit, and an energy storage system to deliver efficient, localized energy generation and management. Within this framework, a Nonlinear Model Predictive Control (NMPC) and an Extended Kalman Filter (EKF) are employed to regulate critical microclimate parameters such as temperature, relative humidity, CO2 concentration, and lighting intensity, while optimally managing energy storage to reduce grid power imports. The NMPC minimizes a cost function encompassing multiple objectives and constraints, whereas the EKF enhances control precision by addressing measurement errors and model noise. Simulations revealed that the SGIM met over 83% of its energy needs through local generation, with only 3.8% sourced from the external grid. This approach offers an effective solution for achieving near-zero energy consumption in sustainable agriculture, with scalability for various greenhouse types and sizes.

INDEX TERMS Smart greenhouse, microgrid, renewable energy, energy efficiency.

NOMENCLATURE

SYSTEM VARIABLE

Bat_{SOC}	Battery stage of charge [%].
$C_{CO2,i}$	Indoor CO_2 concentration [ppm].
I_l	Indoor light intensity [μmol/(sm^2)].
Rh_i	Indoor relative humidity [%].
T_i	Indoor temperature [^{o}C].

AMBIENT VARIABLE

G_{sr}	Global Solar irradiation [W/m^2].
Rh_a	Ambient relative humidity [%].
T_a	Ambient temperature [^{o}C].
v_{wind}	Wind speed [m/s].

PARAMETERS

A_f	Greenhouse floor surface [m^2] 42.
A_{hmax}	Maximum capacity of battery [Ah] 100.

A_{pv}	Solar panel area [m^2] 40.
A_v	Area of open window [m^2] 1.
C_a	Specific heat capacity of air [W/(kgK)] 1005.

CONTROL VARIABLES

I_{chg}	Battery charging current [A].
I_{dis}	Battery discharging current [A].
Q_s	Heating supply of micro-CHP [W].
u_{al}	Operational status of supplemental lighting, $0 \le u_{al} \le 1$.
u_{CO2}	Operational status of CO_2 injector, $0 \le u_{CO2} \le 1$.
u_{deh}	Operational status of dehumidifier, $0 < u_{deh} < 1$.
u_{fog}	Operational status of fogging system, $0 \le u_{fog} \le 1$.
α	Ventilation open angle [^{o}], $0 \le \alpha \le 44$.
n_r	Number or hot water radiator [unit] 2.
P_a	Atmospheric air pressure [Pa] 101325.
P_{al}	Power rating of lamp [W] 2500.
P_f	Packing factor [pu] 0.83.
P_{deh}	Power rating of dehumidifier [W] 1100.
$C_{CO2,o}$	Outdoor CO_2 concentration [ppm] 420.

C_r	Specific heat of radiator wall [J/(kgK)] 447.	
C_w	Specific heat of water [J/(kgK)]] 4186.	
D	Hydraulic diameter of pipe [m^2] 0.1128.	
E	Evapotranspiration rate of plants in greenhouse [pu] 0.5.	
H	Height of the greenhouse [m] 3.5.	
$I_{chg,max}$	Battery maximum charging current [A] 15.	
$I_{dis,max}$	Battery maximum discharging current [A] 15.	
I_{ll0}	Light output rating of artificial lighting [μmol/(sm^2)] 200.	
K_1	Constant 100.	
K_2	Constant [Pa] 1.7001.	
K_3	Constant [Pa]; 7/7835.	
K_4	Constant [1/K] 1/17.0789.	
K_5	Constant [kg$_w$/kg$_a$] 0.6228.	
K_6	Coefficient associated with the respiration rate of the crop [^{o}C] -0.27.	
K_7	Coefficient associated with the respiration rate of the crop (no dim.) 0.05.	
K_i	Thermal conductivity of hot water [W/(mK)] 0.64.	
$K_{inj,max}$	Max carbon injected by CO_2 generator [kg/m^2] 0.8e-3.	
K_{le}	Efficiency of conversion visual light to PAR 0.5.	
$K_{ph,max}$	Photosynthesis coefficient of the crop [kg/(Wh)].	
$K_{res,max}$	Respiration coefficient of the crop [kg/(m^{2}hK)] 1.224e-6.	
L_p	Equivalent pipe length [m] 3.5.	
m_r	Weight of radiator [kg] 97.	
m_w	Volume flow rate of hot water [m^3/s] 0.000667.	
N	Greenhouse infiltration rate [1/h] 0.75.	
N_c	Control horizon of NMPC, 3.	
N_p	Prediction horizon of NMPC, 18.	
P_{fog}	Power rating of fogging system [W] 1100.	
P_{fan}	Power rating of circulation fan [W] 370.	
P_{pump}	Power rating of hot water pump [W] 185.	
P_r	Prantl number of waters at 50 ^{o}C 3.559.	
$Q_{s,max}$	Micro-CHP maximum heating output [W] 23100.	
$Q_{s,min}$	Micro-CHP maximum heating output [W] 4100.	
Bat_{SOCmax}	Battery maximum stage of charge [%] 90.	
Bat_{SOCmin}	Battery minimum stage of charge [%] 10.	
S_r	Surface area of radiator [m^2] 5.	
T_s	Time step of controller [s] 600.	
$T_{w,max}$	Maximum temperature of water [^{o}C] 60.	
$T_{w,min}$	Minimum temperature of water [^{o}C] 35.	
U	Overall heat transfer coefficient of greenhouse [Wm^2/K] 2.2713.	
V_a	Greenhouse volume [m^3] 212.5.	
V_w	Capacity of Thermal Storage System (TSS) [m^3] 1.	
$W_{deh,max}$	Max rate of dehumidifier [kg/(m^{2}h)] 1.6.	
W_{evp}	Evaporation rate of the crop [kg/(m^{2}h)] 0.1258.	
$W_{fog,max}$	Max vapor rate of fogging systems [kg$_W$/(m^{2}h)] 0.0096.	
β_{chg}	Efficiency of charging the battery 0.9.	
β_{dis}	Efficiency of discharging the battery 0.9.	
η_{pc}	Power conditioning efficiency 0.9.	
η_{pv}	Efficiency of the solar panel 0.2.	
ρ_a	Gravity density of air [kg/m^3] 1.207.	
$\Delta Q_{s,max}$	Micro-CHP maximum ramp rate of heating output [W/s].	
$\Delta Q_{s,min}$	Micro-CHP minimum ramp rate of heating output [W/s].	

I. INTRODUCTION

Traditional farming methods are increasingly being supplemented by technological innovations such as greenhouses, which provide controlled environments to optimize crop production. However, the energy demands of greenhouse operations, particularly for climate control, pose new challenges. As energy costs increase and environmental concerns regarding carbon emissions grow, there is a critical need for more sustainable and energy-efficient greenhouse management solutions. Smart agriculture leverages technologies such as automation, intelligent control, and energy management to address these challenges. By integrating energy-efficient management systems, smart agriculture can reduce costs and improve sustainability while ensuring optimal growth conditions [1]. Smart greenhouses, as crucial components of modern agricultural practices, must adopt advanced technologies to thrive in an era of resource constraints.

Simultaneously, the rise of microgrids offers a promising solution to this energy dilemma. Microgrids are localized energy systems capable of operating independently or in conjunction with the main power grid. They are particularly suited for settings such as greenhouses, which have specific energy demands and often need to be operated in remote or semi-remote areas. The integration of renewable energy sources, such as photovoltaic (PV) panels, into microgrids allows for the efficient use of green energy, reduces reliance on fossil fuels and enhances sustainability [2]. The need for sustainable energy systems in agriculture is underscored by increasing regulatory pressure to reduce greenhouse gas emissions, as well as a societal push towards environmentally friendly farming practices. In this context, microgrids offer a resilient and energy-efficient alternative for agricultural settings, especially when combined with intelligent control systems to dynamically manage energy consumption.

The greenhouse microclimate includes essential parameters, such as artificial lighting, temperature, relative humidity, and CO_2 concentration. Optimal ranges vary based on the plant type and growth stage, such as seeding, flowering, or fruiting [3]. In a smart greenhouse, there are wireless sensor networks (WSN), and the Internet of Things (IoT) which allow information about outside weather and the

microclimate to be sampled, stored, and shared between devices to help the operator of the greenhouse monitor, and control the microclimate. For example, in [4], data are collected and transmitted wirelessly, and growers can monitor greenhouse conditions remotely and control systems via smartphones or computers, improving accessibility and response times.

The utilization of local sustainable energy in greenhouses has diversified significantly, driven by technological advancements and growing emphasis on energy sufficiency. Solar energy remains a primary resource; however, its application has expanded beyond traditional rooftop PV panels. For example, semi-transparent organic solar cells (OSCs) [5] represent a novel approach that allows for simultaneous electricity generation and light transmission for plant growth. This dual functionality highlights the trend towards synergistic energy and crop production systems. Trigeneration systems powered by solar energy offer a comprehensive solution by generating electricity, heating, and cooling within greenhouses, thereby reducing reliance on external grids [6]. The integration of PV panels with a Proton Exchange Membrane Fuel Cell (PEMFC) adds another layer of energy independence, which utilizes excess solar energy to produce hydrogen for on-demand power generation [7]. Geothermal energy, accessed through ground source heat pumps (GSHPs), provides another avenue for local energy utilization, particularly for efficient heating and cooling [8]. These diverse approaches demonstrate the expanding potential for local sustainable energy integration in greenhouses, creating a pathway towards a more resilient and environmentally friendly agricultural sector.

From the perspective of energy management and microclimate control in greenhouses powered by microgrids, model predictive control (MPC) has emerged as the dominant approach. Hussain et al. [9] investigated the challenges of operating greenhouses in islanded mode and proposed robust optimization strategies and a precedence methodology to prioritize essential control parameters based on plant growth requirements. This study establishes the importance of considering both grid-connected and islanded scenarios when designing microgrid systems for greenhouses. Achour et al. [10] incorporated the food-energy-water nexus into their Supervisory MPC scheme, optimizing the greenhouse microclimate while minimizing resource consumption. The transition from individual to interconnected greenhouses has marked a significant step towards enhancing sustainability. Ouammi et al. [11] introduced a centralized MPC approach for coordinating energy and water management across multiple greenhouses, demonstrating the benefits of networked operations for maximizing resource utilization and improving energy efficiency. Ouammi [12] expanded this concept further by proposing a framework for achieving net-zero energy consumption in a cluster of interconnected microgrids powering multiple smart greenhouses. The concept of cooperative energy management within these clusters

allows for efficient power exchanges between microgrids to balance supply and demand and reduce reliance on the main grid. Rezaei et al. [13] introduced a hierarchical distributed energy management framework that integrates demand response capabilities into greenhouse networks, allowing them to actively participate in grid services while optimizing their individual energy consumption. This shift towards demand-responsive greenhouses paves the way for greater integration of agricultural systems into the smart grid.

Existing MPCs for smart greenhouse-integrated microgrid (SGIM) often rely on linearized models or neglect system nonlinearities [9], [10], [11], [12], [13]. However, the SGIM is inherently nonlinear, with complex interactions between microclimate variables and environmental parameters. Moreover, although previous studies have addressed uncertainties in renewable production related to environmental conditions, they often overlooked model noise and output measurement errors which are inevitable in practical applications.

To fill these gaps, this study integrates a nonlinear model predictive control (NMPC) with an extended Kalman filter (EKF) for an SGIM, offering a comprehensive approach to manage nonlinearities, and uncertainties. The originality of this work is underscored by the following innovations.

- **Application to a Smart Greenhouse Integrated into a Microgrid (SGIM)**: This study targets a smart greenhouse operating within a microgrid environment, incorporating photovoltaic power, a micro-combined heat and power (micro-CHP) unit, and an energy storage system to optimize energy use, and climate control.
- **Focus on Near-Zero Energy Consumption**: This framework not only optimizes the microclimate for agricultural productivity but also prioritizes energy sustainability, aiming for near-zero energy consumption by reducing dependency on the power grid, and minimizing energy consumption.
- **Seamless Integration of NMPC and EKF**: This study combines NMPC's ability to handle nonlinear dynamics with EKF's strength in filtering measurement errors and model noise. The proposed approach provides more reliable control actions, ensuring the system stability and optimal performance
- **Simulation-based Validation:** The methodology was tested through realistic simulations of an SGIM that was developed using Multiphysics modeling in MATLAB/ Simulink. This simulator integrates different physical domains including thermal fluid, air moisture, and electrical domains, providing an integrated environment, offering practical insights and demonstrating the effectiveness of the approach.

This novel framework bridges the gap between theoretical advancements in MPC and practical greenhouse management requirements, offering a resilient and integrated solution. Different to previous work, this study addresses system nonlinearities and complex interactions between microclimate variables, which are often oversimplified in linear models.

In addition, by explicitly targeting model noise and measurement errors, this study paves the way for more reliable and efficient control of smart greenhouses in practice.

The remainder of this paper is organized as follows: The Methodology section describes the system model, which includes the greenhouse microclimate, PV power generation, micro-CHP unit, artificial lighting, and energy storage system. Next, we present a nonlinear control framework, detailing the NMPC design, its state-space representation, objective functions, constraints, and the EKF. The Simulation and Discussion section demonstrates the effectiveness of the NMPC combined with the EKF in regulating the greenhouse microclimate and the energy storage system. Finally, the Conclusion highlights the limitations of this study and outlines the directions for future research.

II. SYSTEM MODEL AND CONTROL ALGORITHM

A. SYSTEM MODEL

The microgrid model integrates a greenhouse with renewable energy sources and energy storage. The microgrid connects to the main grid allowing bilateral electricity trading. It includes photovoltaic (PV) panels for solar power generation, a micro-CHP unit to supply electricity and heat, and a battery system for energy storage. The microgrid is designed to manage the energy needs of the greenhouse and maintain both energy efficiency and a microclimate favorable for plant development. This setup allows for the coordination of power generation and storage to meet varying demands, ensuring a stable and eco-friendly energy supply. Fig.1 shows the layout of the proposed microgrid.
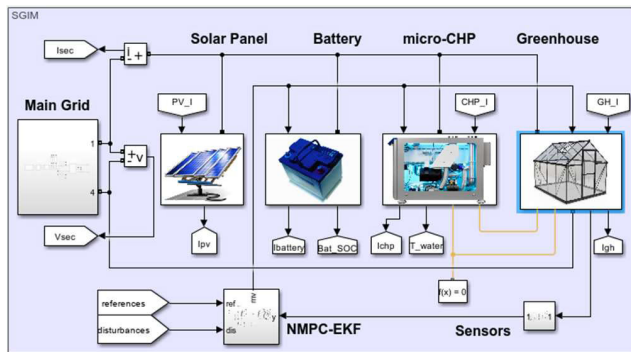

FIGURE 1. Layout of the smart greenhouse integrated microgrid.

1) HEATING MODEL

This heating model is based on the condition that the micro-CHP system always operates to satisfy the heating demands of the greenhouse. The heating supply to the greenhouse is controlled by regulating the heating output of the micro-CHP. The dynamic temperature of the greenhouse air follows the energy transfer and mass balances, which can be expressed as

$$Q_{gain} - Q_{loss} = C_a \rho_a V_a \frac{dT_i}{dt} \tag{1}$$

where, T_i is the indoor air temperature (°C), C_a is the specific heat capacity of air (W/(kgK)), ρ_a is the gravity density of dry air (kg/m^3), V_a is the total volume of dry air inside the greenhouse (m^3), Q_{gain} is the sum of thermal energy entering the greenhouse (W), and Q_{loss} is the sum of thermal energy exiting the greenhouse (W).

The total thermal energy loss in the greenhouse consists of heat loss by conduction, convection and radiation due to temperature differences with the environment, heat loss by infiltration, and heat loss due to natural ventilation

$$Q_{loss} = Q_{rc} + Q_{inf} + Q_{ven} \tag{2}$$

The heat loss to the environment is composed of heat losses due to radiation, conduction, and convection, Q_{rc} is calculated as [14]:

$$Q_{rc} = US(T_i - T_a) \tag{3}$$

where U is the overall heat transfer coefficient which depends on glazing method and materials of the greenhouse (W/m^{2}K)), S is the area of the cover (m^2), T_i is the temperature inside the greenhouse (°C), and T_a is the ambient temperature (°C).

The heat loss due to air infiltration in the greenhouse is calculated as [14]:

$$Q_{inf} = \rho_a V_a N[C_a(T_i - T_a) + h_{fg}(W_i - W_o)] \tag{4}$$

where V_a is the volume of air inside the greenhouse (m^3), N is the infiltration rate (1/s), ρ_a is the density of greenhouse air (kg/m^3), C_a is the specific heat capacity of air (W/(kgK)), h_{fg} is the latent heat of vaporization of water at T_i (J/kg), W_i is the humidity ratio of the inside air (kg$_{water}$/kg$_{air}$), and W_o is the humidity ratio of the outdoor air (kg$_{water}$/kg$_{air}$).

In this model, a natural ventilation window is used when the greenhouse is overheated. The total heat loss due to the operation of the ventilation window can be calculated as:

$$Q_{ven} = \rho_a V_a N_{ven}[C_a(T_i - T_a) + h_{fg}(W_i - W_o)] \tag{5}$$

where N_{ven} is the air exchange rate (1/s), depending on the wind speed outside, and the type of ventilator window, N_{ven} can be calculated from [11]

$$N_{ven} = 3600 A_v v_{wind} G(\alpha) \tag{6}$$

where A_v is the ventilation window area (m^2), v_{wind} is the outside wind speed (m/s), and G (α) is a function of the opening angle window α (°), which is determined by:

$$G(\alpha) = 2.29 * 10^{-2} * (1 - \exp\left(-\frac{\alpha}{21.1}\right)) \tag{7}$$

The heat sources are solar irradiation, the heating effect of artificial light, and the controllable heat source from the micro-CHP.

$$Q_{gain} = Q_{sen} + Q_{al} + Q_{ech} \tag{8}$$

In greenhouses, sensible heat, which is the heat gain from evaporation activity can be estimated using the following equation:

$$Q_{sen} = (1 - E)\tau G_{sr} A_f \tag{9}$$

where E is the evapotranspiration coefficient, which is between 0 and 1, depending upon the crop, and conditions of humidity that contribute to evaporation inside the greenhouse, τ is the solar transmissivity of cover, G_{sr} is the global horizontal radiation (W/m^2), and A_f is the area of greenhouse floor (m^2).

$$Q_{al} = (1 - \eta_{al})P_{al}u_{al} \tag{10}$$

where η_{al} is the efficiency of the artificial lighting system, P_{al} is the rated power of the artificial lighting (W/m^2), and u_{al} is the operational status of the artificial light system.

The heat supplied from the micro-CHP through the Thermal Storage System (TSS), and hot water radiators can be expressed by the following equations:

$$Q_{ech} = n_r k_r A_r (T_H - T_i) \tag{11}$$

$$Q_{tss} - Q_{ech} = n_r C_r m_r \frac{dT_H}{dt} \tag{12}$$

$$Q_s - Q_{tss} = C_w \rho_w V_w \frac{dT_w}{dt} \tag{13}$$

where Q_{ech} is the convection heat transfer from radiator to air (W), n_r is number of radiators, k_r is the convection heat transfer coefficient (W/(m^{2}K)), A_r is the surface area of radiator (m^2), T_H is the temperature at of the radiator wall (^{o}C), T_i is the indoor temperature (^{o}C), Q_{tss} is the heat transferring from TSS through radiators via water pump, and Q_s is supplying heat from the micro-CHP (W).

The heat transfer from the TSS to the radiator tank via hot water using a water pump was modeled as heating transfer via a heating pipe. The heat is the sum of the conduction heat and the convection heat, which is calculated as follows:

$$Q_{tss} = n_r * \left\{ \frac{k_I S_H}{D} (T_w - T_H) \right.$$
$$\left. + C_w m_w \left(1 - e^{\frac{-hS_H}{C_w m_w}} \right) (T_w - T_H) \right\} \tag{14}$$

where D is the hydraulic diameter (m), k_I is the thermal conductivity of the hot water (W/ (mK)), defined internally for each pipe segment, S_H is the surface area of the pipe wall, T_H is the pipe wall temperature (^{o}C), T_w is the hot water temperature (^{o}C), and the heat transfer coefficient is:

$$h = \frac{N_u k_{avg}}{D} \tag{15}$$

where k_{avg} is the average thermal conductivity of the thermal liquid over the entire pipe (W/(mK)), N_u is the average Nusselt number in the pipe, calculated using the Dittus-Boelter correlation as [15]

$$N_u = 0.023 R_e^{0.8} P_r^{0.4} \tag{16}$$

where R_e is Reynolds number, and P_r is the Prandtl number respectively.

The main heating source in this model is the micro-CHP which is proposed because of its ability to maximize energy efficiency by producing both heat and electricity from a single fuel source. This approach significantly reduces energy waste by recovering heat from exhaust gases, while also supporting localized energy production, and decreasing dependency on external power grids. On the electrical side, the micro-CHP also offers the potential to sell excess electricity to the main grid. This dual benefit makes them a highly efficient and economically viable solution for greenhouse energy management [16].

In the model, we implemented a micro-CHP system using Internal Combustion Engine (ICE) technology. The heating output is generated by recovering heat from exhaust gases, which are then used to heat the water stored in a TSS. The control strategy was designed to regulate the heating output to meet the greenhouse heating demand, whereas the electrical output was determined using a lookup table, $P_{CHP} = f(Q_s)$. Fig. 2 shows the micro-CHP and TSS model.

The heating supply by the micro-CHP system and its ramp rate are subject to the following constraints:

$$Q_{s,\min} \leq Q_s(t) \leq Q_{s,\max} \tag{17}$$
$$\Delta Q_{s,\min} \leq \Delta Q_s(t) \leq \Delta Q_{s,\max} \tag{18}$$

The temperature of hot water is subject to its working temperature range:

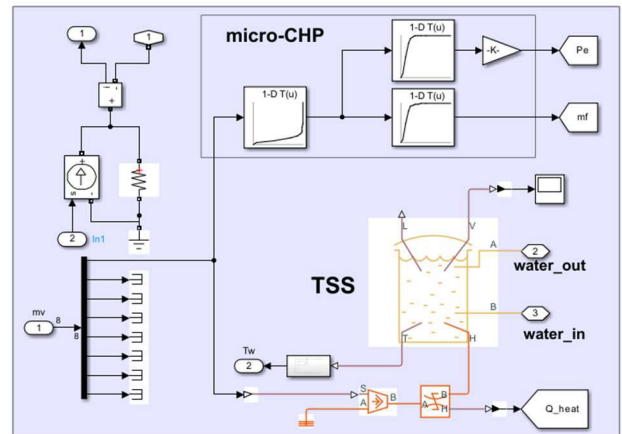$$T_{w,\min} \leq T_w(t) \leq T_{w,\max} \tag{19}$$

FIGURE 2. Micro-CHP and TSS model.

2) RELATIVE HUMIDITY

Relative humidity is an important parameter in the microclimate inside a greenhouse, and is defined as:

$$Rh_i(t) = \frac{P_{par}(t)}{P_{sat}(t)} * 100\% \tag{20}$$

where saturated pressure and partial pressure can be estimated by:

$$P_{sat}(t) = K_1(-K_2 + K_3 e^{K_4 T_i}) \quad (21)$$

$$P_{par}(t) = \frac{W_{in} P_a}{K_5} \quad (22)$$

The water content of the indoor air W_i is modeled based on the mass balance theory, considering the moisture ventilated by natural air ventilation and the water quantity added or removed by the fogging system or dehumidifier, as follows

$$\frac{dW_i}{dt} = \frac{A}{\rho_a V_a}[W_{evp} + \rho_a \frac{V_a}{A} N_{ven} (W_o - W_i)$$
$$+ u_{fog} W_{fog,max} - u_{deh} W_{deh,max}] \quad (23)$$

where ambient water content W_o can be calculated approximately by:

$$W_o = \frac{K_5 Rh_a K_1(-K_2 + K_3 e^{K_4 T_a})}{P_a} \quad (24)$$

Relative humidity revolution can be derived as below equation

$$\frac{dRh_i}{dt} = \frac{P_a}{C_5 P_{sat}} \frac{dW_i}{dt} - \frac{Rh_i}{P_{sat}} \frac{dP_{sat}}{dt} \quad (25)$$

where:

$$\frac{dP_{sat}}{dt} = K_1 K_3 K_4 e^{K_4 T_i} \frac{dT_i}{dt} \quad (26)$$

The relative humidity, and operation status of the fogging system and dehumidifier can be constrained between the minimum and maximum values as follows:

$$Rh_{i,min} \le Rh_i (t) \le Rh_{i,max} \quad (27)$$
$$0 \le u_{fog}(t) \le 1 \quad (28)$$
$$0 \le u_{deh}(t) \le 1 \quad (29)$$

Besides, the fogging system and dehumidifier should not operate simultaneously:

$$u_{fog}(t) u_{deh}(t) = 0 \quad (30)$$

3) CO₂ CONCENTRATION

The CO_2 concentration in the greenhouse is mainly influenced by the injected CO_2, and CO_2 consumption by the plants via photosynthesis and exchange with the environment via natural ventilation. The change in the indoor CO_2 concentration is modeled as [10]

$$\frac{dC_{CO2,i}}{dt} = \frac{A_f}{\rho_a V_a}[K_{inj}^{max} u_{CO2}$$
$$+ \rho_a \frac{V_a}{A_f} N_{ven} (C_{CO2,o} - C_{CO2,i})$$
$$+ K_{res}(K_6 + K_7 T_i) - K_{pho} I_l] \quad (31)$$

where $C_{CO2,i}$, $C_{CO2,o}$, and u_{CO2} represent the indoor CO_2 rate, ambient CO_2 rate, and operational status of CO_2 generator, respectively; A_f, V_a, and ρ_a denote the area, air volume of the greenhouse, and air density, respectively; K_{res}, K_{pho},

and $K_{inj,max}$ are the respiration coefficient, photosynthesis coefficient, and maximum carbon injected by CO_2 generator, respectively; and N_{ven} is the ventilation rate of the greenhouse. For simplicity, we assume that the ambient CO_2 concentration, $C_{CO2,o}$, is constant. The indoor CO_2 concentration can be constrained within the boundary values as follows:

$$C_{CO2i,min} \le C_{CO2,i}(t) \le C_{CO2i,max} \quad (32)$$

The operation status of the CO_2 injector is within its operation range

$$0 \le u_{CO2}(t) \le 1 \quad (33)$$

4) SUPPLIMENTAL LIGHTING

The model uses light-emitting diodes (LEDs) as supplemental lighting sources. LEDs are efficient in greenhouse lighting, achieving remarkable energy efficiency by converting up to 49% of the electrical energy into photon energy [17] One of the key advantages of using LEDs is their compatibility with Pulse Width Modulation (PWM) control, which allows for precise regulation of light output [18]. This control approach ensures that plants receive supplemental light only when needed, thereby optimizing energy use while promoting healthy growth. The effectiveness of dynamic lighting control (DLC) further illustrates the benefits of PWM in LED systems. By integrating a quantum Photosynthetically Active Radiation (PAR) sensor and programmable microcontroller, the DLC circuit can intelligently modulate light levels based on real-time conditions. This innovative strategy results in a 20% reduction in electricity consumption compared to traditional lighting systems that operate under a simple on-off regime [19]. The light intensity in the greenhouse includes solar irradiation, and supplemental artificial light.

$$I_l = I_{sl} + I_{al} \quad (34)$$

where I_{sl} is the light intensity gained by solar irradiation:

$$I_{sl} = \tau K_{le} G_{sr} \quad (35)$$

where, G_{sr} is the global solar irradiation (W/m²), K_{le} is the factor of solar irradiation that contributes to PAR, τ is the visual light transmission, and I_{al} is the light intensity produced by artificial lighting, which is modeled as a first-order equation:

$$I_{al} = I_{ll0}\left(1 - e^{-Kt}\right) u_{al} \quad (36)$$

where, I_{ll0} is the light output rating of the artificial lighting system (μmol/(sm²)), u_{al} is the operation status of the artificial lighting, K is a time constant value, K = 2/T_s, and T_s is the time step of the system (s).

Assuming that global solar irradiation is constant during a prediction step, the evolution of the light intensity inside the greenhouse can be expressed as:

$$\frac{dI_l}{dt} = -KI_l + KI_{sl} + KI_{ll0} u_{al} \quad (37)$$

The operation status of the artificial lighting is subject to constrain:

$$0 \leq u_{al}(t) \leq 1 \tag{38}$$

A microclimate model of the greenhouse was created using physical modeling in Simulink/Simcape. The heating system was modeled with the fluid domain, while the greenhouse air volume was represented using the Moist Air domain. This approach allows for the description of the physical structure of the system, rather than relying on the underlying mathematical equations. A model of the greenhouse microclimate is shown in Fig. 3.
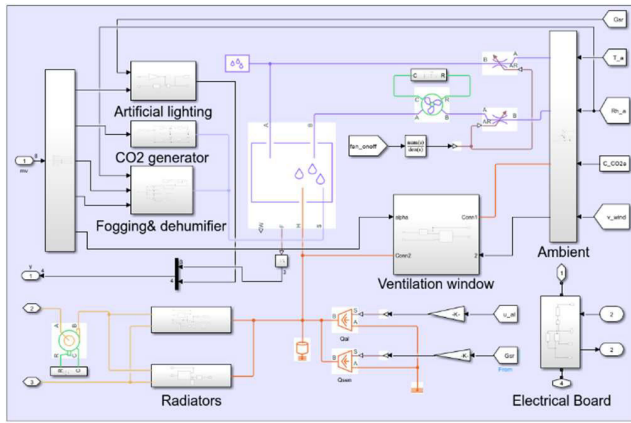
FIGURE 3. Greenhouse microclimate model.

5) PV POWER

The photovoltaic (PV) power produced can be calculated as follows [12]:

$$P_{pv} = A_{pv}\eta_{pv}P_f\eta_{pc}G_{sr} \tag{39}$$

where A_{pv} is the solar panel area (m^2), η_{pv} is the efficiency of the solar panel, P_f is the packing factor, η_{pc} is the power conditioning efficiency, and G_{sr} is the global solar irradiation (W/m^2).

6) ENERGY STORAGE SYSTEM

The battery stage of charge can be modeled as [11]

$$Bat_{SOC}(t) = Bat_{SOC0} + \frac{\int \beta_{chg}I_{chg}dt}{Ah_{max}} - \frac{\int I_{dis}dt}{\beta_{dis}Ah_{max}} \tag{40}$$

where I_{chg}, I_{dis} are the charging and discharging currents (A), respectively; β_{ch}, β_{dis} are the charging and discharging efficiencies, respectively; and Ah_{max} is the battery capacity (Ah).

State transition of the battery SOC can be presented as below:

$$\frac{dBat_{SOC}}{dt} = \frac{\beta_{chg}I_{chg}}{Ah_{max}} - \frac{I_{dis}}{\beta_{dis}Ah_{max}} \tag{41}$$

The battery SOC, and currents are subjected to the boundary constraints:

$$Bat_{SOC,min} \leq Bat_{SOC}(t) \leq Bat_{SOC,max} \tag{42}$$

$$I_{chg,min} \leq I_{chg}(t) \leq I_{chg,max} \tag{43}$$

$$I_{dis,min} \leq I_{dis}(t) \leq I_{dis,max} \tag{44}$$

In addition, the charging and discharging processes must not be operated simultaneously

$$I_{chg}(t)\,I_{dis}(t) = 0 \tag{45}$$

The battery is controlled to be charged when there is excess power in the microgrid, and it discharges when the microgrid power is insufficient.

7) POWER BALANCE IN THE MICROGRID

The power balance in the microgrid can be presented as follows:

$$P_{chp} + P_{pv} + P_{dis} + P_{imp} = P_{gh} + P_{chg} + P_{exp} \tag{46}$$

where P_{chp} is the power generated from the micro-CHP, P_{pv} is the power generated from PV panels, P_{dis} is the power discharged from the battery, P_{imp} is the power imported from the grid; P_{gh} is the total load of greenhouse, P_{chg} is the power charging the battery, and P_{exp} is the power exported to the grid.

The total greenhouse load is calculated as follows:

$$P_{gh} = P_{pump} + P_{fan} + P_{al} + P_{CO2} + P_{fog} + P_{deh} \tag{47}$$

where P_{pump} is the power consumed by the water pump (W), P_{fan} is the power consumed by the circulation fan (W), and P_{al} is the power consumed by the artificial lighting system (W), which is proportional to the operational status of the lighting system.

$$P_{al} = \frac{I_{al}}{\eta_{al}}u_{al} \tag{48}$$

where I_{al} (μmol/s) is the lighting output from the lighting system, and η_{al} (μmol/J) is the efficiency of converting electrical power to PAR.

Refer to (47), P_{CO2}, P_{fog}, P_{deh} are the power consumptions of the CO$_2$ injector, fogging system and dehumidifier, respectively. These are calculated as the products of their operational status and the corresponding maximum rating powers.

$$P_{CO2} = P_{CO2,max}u_{CO2} \tag{49}$$

$$P_{fog} = P_{fog,max}u_{fog} \tag{50}$$

$$P_{deh} = P_{deh,max}u_{deh} \tag{51}$$

The power exchanged with the main grid can be written as:

$$P_{ech} = P_{exp} - P_{imp} = P_{net} + P_{dis} - P_{chg} \tag{52}$$

where:

$$P_{net} = P_{chp} + P_{pv} - P_{gh} \tag{53}$$

P_{net} represents the net power generated by the microgrid, excluding storage battery power. We aim to control the battery to maximize local power usage and minimize imports from the main grid. When P_{net} is positive, the microgrid generates more power than the greenhouse's needs, and the excess power either charges the battery or is exported to the grid. When P_{net} is negative, the greenhouse consumes more power than the microgrid's generation, and the battery discharges to supply the deficit, reducing the need to import power from the grid.

B. NMPC-EKF CONTROL ALGORITHM

NMPC optimizes control actions by minimizing a cost function for a constrained system over a receding horizon N_p. At each timestep, the controller evaluates the plant outputs and disturbances, predicts future states based on an internal model, and determines the control actions over a control horizon N_c (where $N_c \leq N_p$) by minimizing the objective function. The first control action is applied, and the process is iteratively repeated at each new step. NMPC can accommodate nonlinear models, inequality constraints, nonlinear constraints, and various cost functions. EKF plays a critical role in estimating the system states and mitigating the effects of process noise and measuring errors, thereby improving the accuracy of the predictions. Fig. 4 shows the control loop of the control framework.
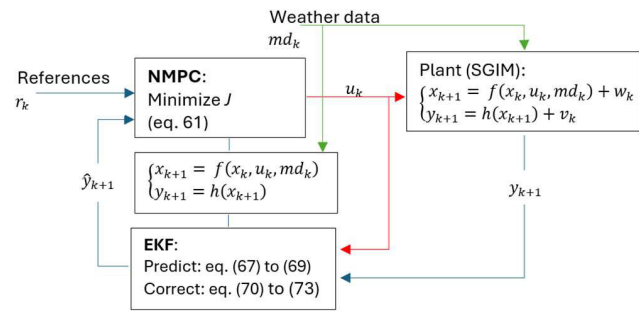
FIGURE 4. Proposed NMPC-EKF control loop for SGIM.

1) NONLINEAR MPC
The NMPC design focuses on multiple objectives:

- Optimizing greenhouse conditions for plant growth by monitoring and adjusting internal variables, such as temperature, relative humidity, CO_2 concentration, and artificial lighting. The goal is to closely follow the reference setpoints while accounting for the complex interactions among variables, fluctuations in renewable resources, and external conditions.
- The energy storage system aims to maximize its SOC to balance renewable energy production and load fluctuations, ensuring a stable power supply. It prioritizes the use of local renewable energy and minimizes reliance on the main grid.

- To reduce power exchange with the main grid, the system focuses on optimizing local energy usage by prioritizing the charging and discharging of the energy storage system to minimize grid imports.
- Minimize the heating consumption of the greenhouse which contributes to the energy efficiency of the greenhouse.

The objective function of NMPC is expressed as follows:

$$
\begin{aligned}
J(z_k) = {} & \sum_{j=1}^{n_y} \sum_{i=1}^{Np} \left[\frac{w_{i,j}^y}{s_{i,j}^y} \left(r_{i,j} - y_{i,j} \right) \right]^2 \\
& + \sum_{j=1}^{n_u} \sum_{i=1}^{Np} \left[\frac{w_{i,j}^{\Delta u}}{s_{i,j}^u} \left(\Delta u_i \right) \right]^2 + \sum_{i=1}^{Np} \left(\frac{w_i^p}{s_i^p} P_i \right)^2 \\
& + \sum_{i=1}^{Np} \left(\frac{w_i^Q}{s_i^Q} Q_i \right)^2 + J(\varepsilon_k)
\end{aligned}
\tag{54}
$$

The first component is the cost of output reference tracking, where N_p is the number of prediction horizon steps, n_y is the number of output variables, $r_{i,j}$, and $y_{i,j}$ are the reference and output of variable j at interval i respectively. The second component is the cost of the move suppression of n_u manipulated variables. The third component is the cost of importing power from main grid, while the fourth component represents the cost of heating consumption. Here, $w_{i,j}^k$, $s_{i,j}^k$ (where $k = y, \Delta u, P, Q$) are the weighting and scaling factors at interval i for the output variables, manipulated variables, imported power, and heating output, respectively. The last term, $J(\varepsilon_k)$, represents the penalty cost of constraint violations.

The set of (1), (12), (13), (25), (31), (37), and (41) define the dynamic model of the system, which can be discretized as a nonlinear time-invariant system. For a given prediction horizon length N_p, a compact form of the model can be expressed as:

$$
x = f(x_0, u, md)
\tag{55}
$$

The system states $\mathbf{x}$ include hot water temperature T_w, temperature of the radiator wall T_H, indoor air temperature T_i, relative humidity Rh_i, indoor CO_2 concentration $C_{CO2,i}$, lighting intensity I_l, and battery SOC Bat_{SOC}. The control inputs $\mathbf{u}$ consists of the micro-CHP heating output Q_s, ventilation open angle α, fogging operation u_{fog}, dehydrating operation u_{deh}, CO_2 injection u_{CO2}, supplemental light u_{al}, charging and discharging currents of the battery I_{chg}, and I_{dis}. The disturbances $\mathbf{md}$ contain solar radiation G_{sr}, ambient temperature T_a, ambient relative humidity Rh_a, and ambient wind speed v_{wind}. $\mathbf{x_0}$ is the initial state of the dynamic model.

The output of the system includes the hot water temperature T_w, indoor air temperature T_i, relative humidity Rh_i, indoor CO_2 concentration $C_{CO2,i}$, lighting intensity I_l, and battery SOC Bat_{SOC}. The output function is given by:

$$
y = h(x)
\tag{56}
$$

We defined constraints for control inputs, ramp rate of control inputs and boundary limit of its system states. The

set of (17), (18), (28), (29), (33), (38), (43), and (44) are the constraints of the manipulated control variables. The set of (19), (32), and (42) present the constraints of state **x**. These constraints can be discretized and presented in the following compact form throughout the entire prediction horizon N_p:

$$G_u u_k \leq g_u \tag{57}$$

$$G_{\Delta u} \Delta u_k \leq g_{\Delta u} \tag{58}$$

$$G_x x_{k+1} \leq g_x \tag{59}$$

where $\mathbf{G_u}$, $\mathbf{g_u}$ are vectors that represent the control input constraint, $\mathbf{G_{\Delta u}}$, $\mathbf{g_{\Delta u}}$ are vectors that represent the boundary limits of the ramp rates of control inputs, and $\mathbf{G_x}$, $\mathbf{g_x}$ are vectors representing the state boundary limits. Equations (30) and (45) define the nonlinear equality constraints of the manipulated variables that have a compact form as follows:

$$ceq(u_k) = 0 \tag{60}$$

The nonlinear optimization problem can be written for a prediction horizon N_p as below:

$$\min_{u_k} J(z_k)$$

$$S.t \begin{cases} x = f(x_0, u, md) \\ G_u u_k \leq g_u \\ G_x \Delta u_k \leq g_{\Delta u} \\ G_x x_{k+1} \leq g_x - \varepsilon \\ \varepsilon \geq 0 \\ ceq(u_k) = 0 \end{cases} \tag{61}$$

We add a vector of slack variables ε to the objective function because there are limitations to the control inputs that could cause the nonlinear optimization problem to become infeasible. Because the slack variables ε are always non-negative (≥ 0), they effectively soften the constraints by providing a "buffer zone." This approach ensures that the optimization problem remains solvable, even if strict adherence to all constraints is impossible in certain situations.

2) EXTENDED KALMAN FILTER

In practical situations, system models (55) and (56) often contain process noise, and measurement errors are inevitable when sensing the output variables. Therefore, it normally considers a discrete system with model uncertainties and sensor errors as follows:

$$x_{k+1} = f(x_k, u_k, md_k) + w_k \tag{62}$$

$$y_{k+1} = h(x_{k+1}) + v_k \tag{63}$$

Here, we assume that w_k is additive noise which accounts for process noise, and v_k is additive noise that accounts for measurement errors. Both w_k and v_k follow Gaussian distributions.

$$w_k \sim (0, Q_k); v_k \sim (0, R_k) \tag{64}$$

where Q_k and R_k are the covariance matrices for model noise and measurement errors, respectively.

The EKF algorithm is based on the linearization of the nonlinear model function, and the measured output function for their most recent estimate states using the Taylor series expansion. The Jacobian matrices of the state function and output function over the estimated states are derived as

$$F_k^{(x)} = \frac{\partial f}{\partial x} f(x_{k|k}, u_k, md_k) \tag{65}$$

$$H_{k+1}^{(x)} = \frac{\partial h}{\partial x} h(x_{k+1|k}) \tag{66}$$

Given an initial state x_0 and covariance P_0, the EKF algorithm has the following expressions [20]

Predict step:

$$x_{k+1|k} = f(x_{k|k}, u_k, md_k) \tag{67}$$

$$P_{k+1|k} = F_k^{(x)} P_{k|k} F_k^{(x)T} + Q_k \tag{68}$$

$$y_{k+1|k} = h(x_{k+1|k}) \tag{69}$$

Correct step:

$$S_{k+1} = H_{k+1}^{(x)} P_{k+1|k} H_{k+1}^{(x)T} + R_{k+1} \tag{70}$$

$$K_{k+1} = P_{k+1} H_{k+1}^{(x)T} S_{k+1}^{-1} \tag{71}$$

$$x_{k+1|k+1} = x_{k+1|k} + K_{k+1}(y_{k+1} - y_{k+1|k}) \tag{72}$$

$$P_{k+1|k+1} = P_{k+1|k} - K_{k+1} S_{k+1} K_{k+1}^T) \tag{73}$$

The selection of covariance matrices Q_k, and R_k significantly affect the performance of the EKF. In the literature, the covariance matrix R_k is typically determined based on the accuracy of the measurement sensors. For uncorrelated sensors, covariance matrix R_k has the form of a diagonal matrix, where each element represents the variance of the sensor's accuracy. It is commonly assumed that the covariance matrix Q_k is diagonal, where each element corresponds to the error variance of a state caused by the process noise [21]. Tuning Q_k can follow a trial-and-error procedure, as described in [22], or auto-tuning techniques can be applied, as presented in [23], [24], [25], and [26]. In this study, we employed an auto-tuning approach using Particle Swarm Optimization (PSO), as proposed in [25]. We select covariance matrix Q_k by minimizing the mean normalized square error (MNSE) calculated as follows:

$$MNSE = \frac{1}{K} \sum_{i=1}^{n_x} \sum_{j=1}^{K} [1/s_i(\hat{x}_{ij} - x_{ij})]^2 \tag{74}$$

where $\hat{x}_{ij}$, x_{ij} are i^{th} predicted state and actual state, respectively at j^{th} sample, s_i is a scale factor of ith state, K is the number of samples, and n_x is the number of states.

III. APPLICATION TO CASE STUDY
A. SIMULATION SETUP
To evaluate the performance of the proposed NMPC-EKF framework, we ran simulations across multiple scenarios. These include a 24-hour operation under ideal conditions (Case Study 1) and a 3-day operation incorporating weather forecast and measurement uncertainties (Case Study 2). In each case study, the length of the prediction horizon and control horizon were set to 3h and 30 min, respectively, with

a control interval of 10 min. The proposed control strategy was applied to an SGIM equipped with a micro-CHP, PV generation, fogging system and dehumidifier, artificial light source, CO_2 generator, battery, and sensors. We considered installing semi-transparent PV panels [27] on rooftop of the greenhouse which offers light transmission coefficient of approximately 0.35. The proposed control strategy is run for an SGIM specialized in the cultivation of lettuce [3] where a day temperature of 25°C and a night temperature of 22°C are optimum for its root growth and plant development, and where a diurnal increase in the indoor CO_2 from its ambient level to 1000 (ppm) is essential for enhancing its growth rate. The adequate relative humidity requirement is approximately 65%, and the light intensity required by photosynthesis is 100 mmol/(sm²) at the plant surface. Note that the initial guess of the states and manipulated variables are assumed to have high accuracy, which is achieved by using the last operating point of the previous simulation as the initial conditions of the next simulation. The SGIM and the NMPC-EKF algorithm were created and simulated using MATLAB/Simulink software. The NMPC optimization problem was solved by the fmincon function using the Sequential Quadratic Programming (SQP) algorithm. The results were achieved by performing simulations with the fixed-step solver Backward Euler at the fundamental time 10 seconds.

To consider measurement errors, we assumed that Gaussian white noise was added to the output measurements. These noises have a zero mean, with a standard deviation of 0.255°C for temperature measurements, 2.55% for CO_2 level, and lighting intensity, and 1.53% for relative humidity, and battery SOC. These standard deviations were derived from the accuracy of the measurement sensors which were 0.5 °C, 3% (relative humidity), 5% (CO_2 concentration), 5% (light intensity), 3% (SOC) for temperature, relative humidity, CO_2 concentration, lighting intensity, and battery SOC, respectively. Fig. 5 shows the white noises of the output variable measurements.

To simulate imperfect prediction when considering forecast errors, Gaussian white noise was added to the environmental data inputs (G_{sr}, T_a, Rh_a, v_{wind}). These noises have a zero mean, with standard deviations of 7.65% of the measured value for solar irradiation, 0.77°C for ambient temperature, 7.65% of the measured value for relative humidity, and 0.92 m/s for wind speed. Two other measured parameters (v_{al}, and P_{net}) were estimated based on forecast environment data and reference settings, or by using feedback signals derived from the model.

B. RESULTS AND DICUSSION

1) CASE 1

This case study illustrates the performance of NMPC without considering prediction errors, and output measurement errors. The simulation was performed for a 24-hour period with the environmental profile shown on Fig. 6. Because model noise and output measurement errors were not
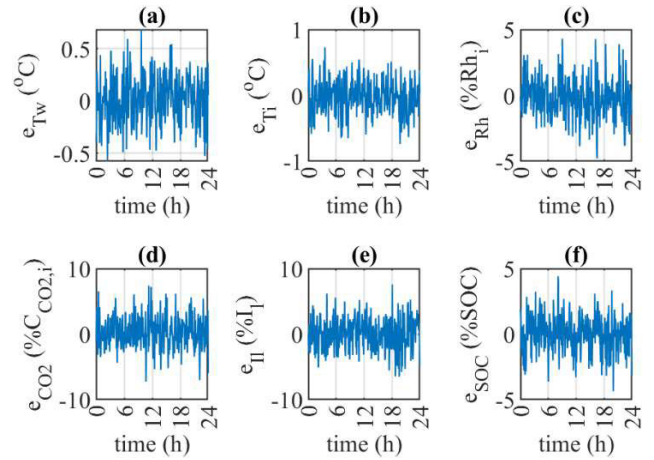

FIGURE 5. Output sensor white noises: (a) Hot water temperature, (b) Indoor temperature, (c) Indoor relative humidity, (d) Indoor CO2 concentration, (e) Indoor lighting intensity, (f) Battery stage of charge.

considered, the covariance matrices Q and R of the EKF were assigned small values as shown in Table 1.

TABLE 1. Covariance matrices in case 1.

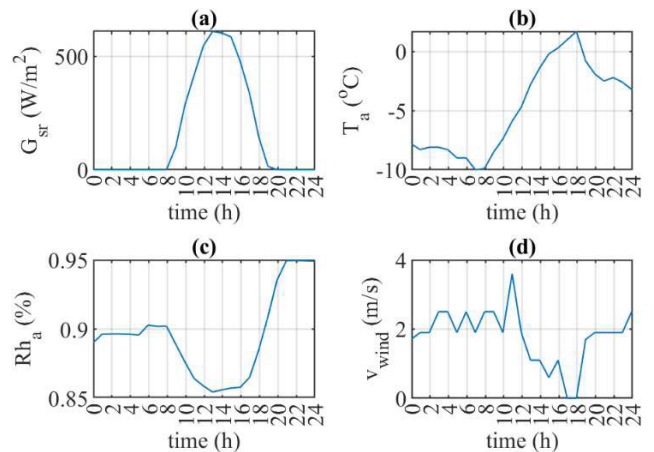| Diagonal elements of the covariance matrix	
Q	$10^{-6}[1, 1, 1, Rh_i^2 10^{-3}, C_{CO2,i}^2 10^{-3}, I_l^2 10^{-3}, SOC^2 10^{-3}]$
R	$10^{-5}[1, 1, Rh_i^2, C_{CO2,i}^2, I_l^2, SOC^2]$

FIGURE 6. Environmental profile used in case study 1: (a) Solar irradiation, (b) Ambient temperature, (c) Relative humidity, (d) Wind speed.

Fig. 7a shows the temperature tracking, where the inside temperature follows reference temperature closely. The heating supplied by the micro-CHP was higher during the early morning hours (0 AM to 4 AM) due to lower ambient temperatures and a lower reference setting of 22°C. The heating output of micro-CHP was reduced gradually from 4 AM

to 6 PM due to the ambient temperature raised, the reference setting increased to 25°C, and solar irradiation along with artificial lighting provided supplement heating to the greenhouse. The natural ventilation window remained closed all the time to limit heating loss. Fig. 7b shows relative humidity tracking where the dehumidifier operated throughout the day to reduce moisture inside greenhouse caused by high ambient relative humidity. Fig. 7c illustrates the CO_2 concentration and the operational status of CO_2 injector. From 0 AM midnight to 4 AM, the plants were resting, and supplement of CO2 was not necessary, resulting in lower operational status of CO2 injector. Fig. 7d shows the lighting intensity. From 0 AM to 4 AM, the artificial lighting was off to allow the plants to rest. Starting from 4 AM, the artificial light was activated to facilitate photosynthetic process. Between 8AM and 6PM artificial lighting decreased when there was natural light in this period.

Fig. 7e illustrates the battery SOC and battery operation currents. The battery was charged in two periods: from 0 AM to 4 AM, and from 10 AM to 6 PM, when there was excess power generated from the micro-CHP and/or the solar panels. The battery was discharged from 4 AM to 10 AM, and from 6PM to midnight due to a power deficit in the microgrid. The efficiency operation of the battery reduced the amount of power imported from the main grid. Additionally, the constraints on the battery SOC boundary limits were satisfied.

Fig. 7f shows the mean absolute errors (MAE) and standard deviation (STD) of the variables in this case. The MAE values for indoor temperature, relative humidity, CO_2 concentration, and lighting intensity were 0.45°C, 1.17%, 33.73 ppm and 4.05 $\mu mol/(sm^2)$ respectively. The MAE of the battery SOC was 37.08%, indicating that, on average, the battery SOC was maintained at 37.08% below its reference setting, because the battery was controlled to discharge power to reduce imported power from the main grid, thereby illustrating the efficiency of battery use. The MAE of the imported power (P_{imp}) was 0.21 kW, indicating that, on average, the microgrid imported 0.21 kW, corresponding to a total of approximately 4.8 kWh over the day. The MAE of the heating supply (Q_s) was 7.99 kW_{th}, meaning that, on average, the micro-CHP supplied 7.99 kW_{th} above its lower bound limit ($Q_{s,min}$ = 4.1kW_{th}). The total heat supplied by the micro-CHP in this case amounted to 290.4 $kW_{th}h$.

Fig. 8 depicts the power balance within the microgrid. The greenhouse load (P_{gh}) increased between 4AM and midnight due to the operation of artificial lighting and the CO2 injector. During the period from 9AM to 3PM, when solar irradiation was at its peak, the local power production reached its highest levels. This excess energy was used to charge the battery, with any remaining surplus exported power to the main grid. The power imported from the grid was needed during the period of 9PM to midnight due to the high load, driven primarily by the increased operation of CO_2 injector, and the battery had been discharged to lower level.

2) CASE 2

In this case, we extended the simulation to cover three consecutive days by considering measurement errors, and weather forecast errors. By introducing these uncertainties, we estimated covariance matrices Q and R of the EKF, allowing it to operate effectively alongside the NMPC. The environmental profile for this case is shown in Fig. 9.

The covariance matrix of the measurement noise, R, was estimated based on the sensor accuracy of the output signals. R was structured as a 6×6 diagonal matrix, where each element on the diagonal represents the variance of each measurement error—calculated as the square of the corresponding standard deviation: R = diag(0.255^2, 0.255^2, $(2.55\% Rh_i)^2$, $(2.55\% C_{CO2,i})^2$, $(2.55\% I_l)^2$, $(1.53\% SOC)^2$), where Rh_i, $C_{CO2,i}$, I_l and SOC are actual values of relative humidity, CO_2 concentration, light intensity, and battery SOC, respectively.

The process noise covariance matrix Q was a 7×7 diagonal matrix, given by Q = diag (q_{Tw}, q_{Th}, q_{Ti}, q_{Rhi}, q_{CCO2}, q_{Il}, q_{SOC}), where the temperature errors due to process noise were directly added to the actual temperature values, while the errors in the other parameters were proportional to their actual values. Table 2 shows the Mean Normalized Square Error (MNSE) values obtained by manually selecting various process noise variances for Q (case 2a to 2e).

TABLE 2. MNSE at difference process noise variances.

Case	Process noise Variances [q_T, q_{Rhi}, q_{CCO2}, q_{Il}, q_{SOC}]	MNSE
2a	[10^{-6}, $Rh_i^2 10^{-9}$, $C_{CO2,i}^2 10^{-9}$, $I_l^2 10^{-9}$, $SOC^2 10^{-9}$]	3.7684
2b	[10^{-5}, $Rh_i^2 10^{-8}$, $C_{CO2,i}^2 10^{-8}$, $I_l^2 10^{-8}$, $SOC^2 10^{-8}$]	3.7859
2c	[10^{-4}, $Rh_i^2 10^{-7}$, $C_{CO2,i}^2 10^{-7}$, $I_l^2 10^{-7}$, $SOC^2 10^{-7}$]	3.7785
2d	[0.5, $Rh_i^2 10^{-3}$, $C_{CO2,i}^2 10^{-3}$, $I_l^2 10^{-3}$, $SOC^2 10^{-3}$]	5.9450
2e	[1.0, $Rh_i^2 10^{-2}$, $C_{CO2,i}^2 10^{-2}$, $I_l^2 10^{-2}$, $SOC^2 10^{-2}$]	6.3905
2*	[3.10^{-5}, $2Rh_i^2 10^{-9}$, $2C_{CO2,i}^2 10^{-9}$, $2I_l^2 10^{-9}$, $2SOC^2 10^{-9}$]	3.7355

To find optimal variances (q_T, q_{Rhi}, q_{CO2}, q_{Il}, q_{SOC}), we employed the PSO algorithm aimed at minimizing the MNSE. The values of process noise covariance were assumed to fall within the lower bound, [10^{-6}, $Rh_i^2 10^{-9}$, $C_{CO2,i}^2 10^{-9}$, $I_l^2 10^{-9}$, $SOC^2 10^{-9}$] (case 2a) and the upper bound [10^{-4}, $Rh_i^2 10^{-7}$, $C_{CO2,i}^2 10^{-7}$, $I_l^2 10^{-7}$, $SOC^2 10^{-7}$] (case 2c). The resulting optimized process noise variances are shown as case 2* in Table 2.

We ran simulations for case 2e (non-tuned EKF) and case 2* (tuned-EKF) and compared the MAEs of the tracking variables between these cases. Table 3 shows that, in the
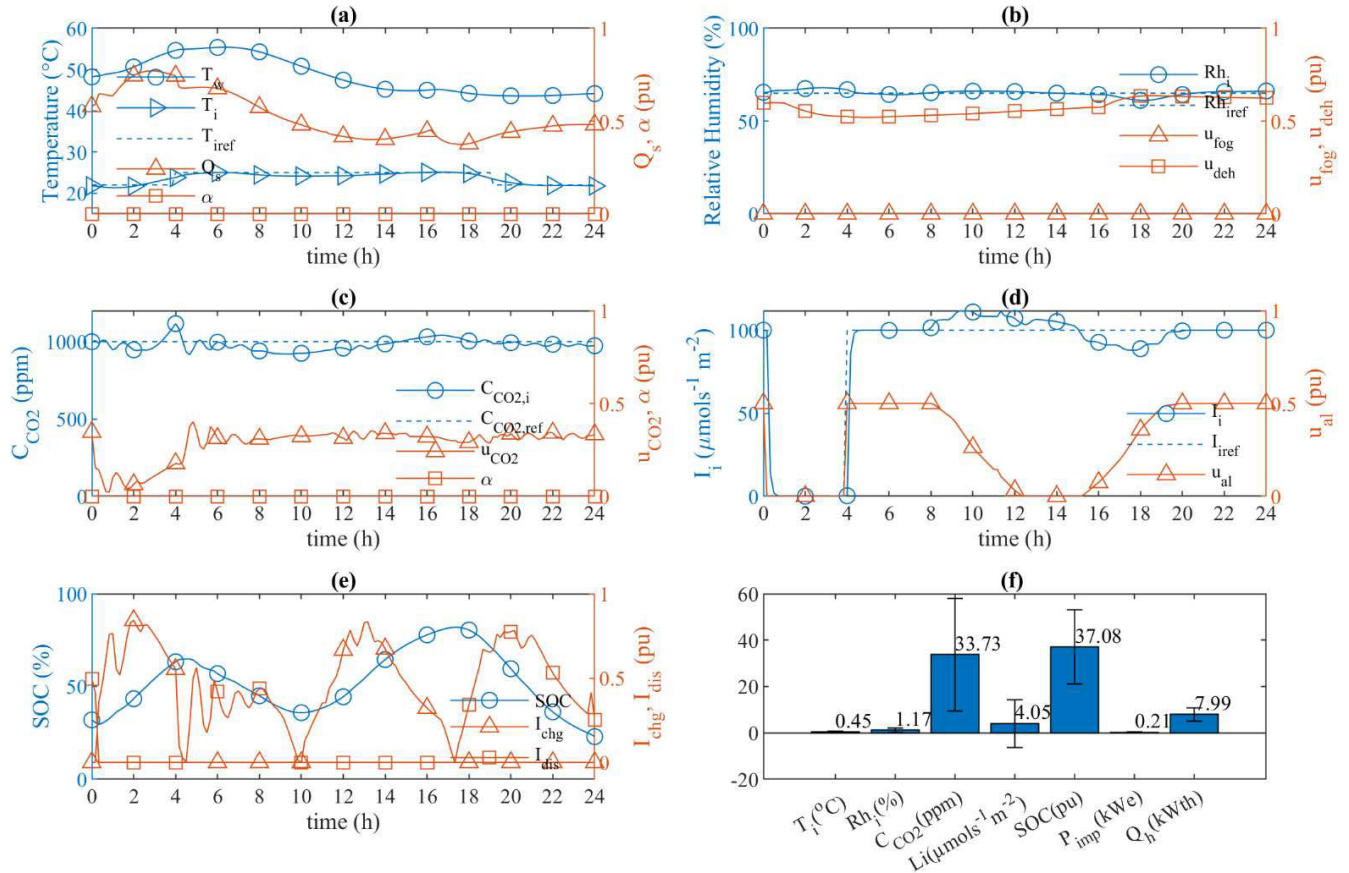
FIGURE 7. Output variable tracking in case study 1: (a) Indoor Temperature, (b) Indoor relative humidity, (c) Indoor CO_2 concentration, (d) Indoor lighting intensity, (e) Battery SOC, (f) MAE of variables; (a)- (e): Left axes: output variables, right axes: control variables.
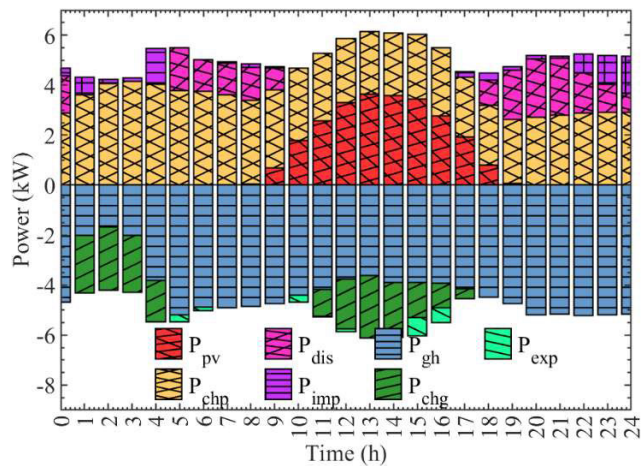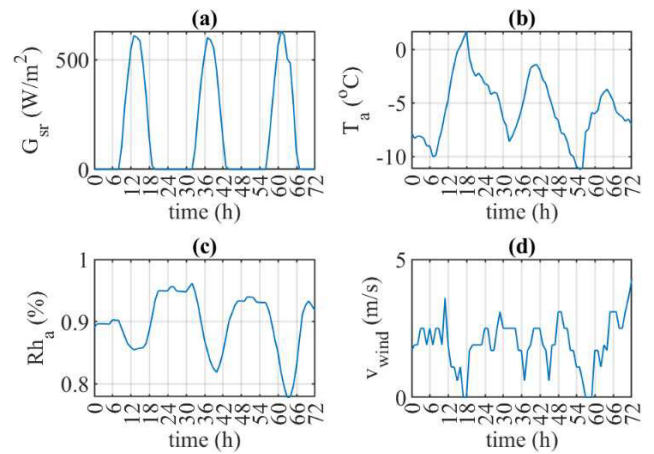

FIGURE 8. Microgrid power balance in case study 1.

FIGURE 9. Environmental profile in case study 2: (a) Solar irradiation, (b) Ambient temperature, (c) Relative humidity, (d) Wind speed.

non-tuned EKF case, there were significantly larger errors in CO_2 concentration tracking and imported power from the main grid compared to those in the tuned-EKF case. For other parameters such as temperature, relative humidity, lighting intensity, and battery SOC, the tracking errors were similar in both cases. These results demonstrate that the tuned EKF

enhances the controller's performance by improving the accuracy of CO_2 concentration and grid power import tracking, indicating its effectiveness in reducing errors and optimizing control.

The control system effectively managed the greenhouse's microclimate maintaining close alignment with their
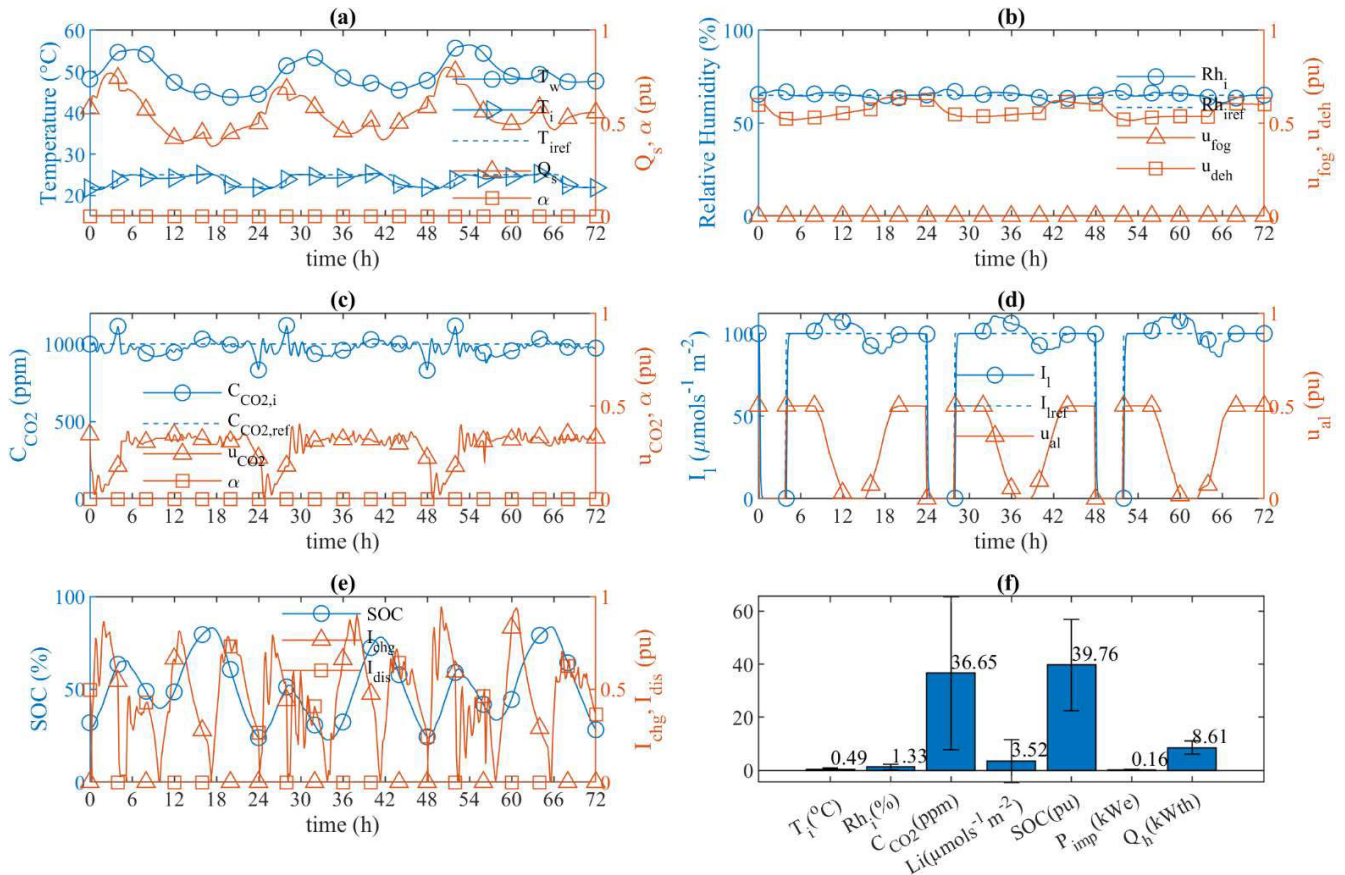
FIGURE 10. Output variable tracking in case 2*: (a) Indoor Temperature, (b) Indoor relative humidity, (c) Indoor CO2 concentration, (d) Indoor lighting intensity, (e) Battery SOC, (f) Mean absolute error of variables; (a)-(e): Left axes: output variables, right axes: control variables.

TABLE 3. Mean absolute errors of variables.

Variables	Case 2e	Case 2*
T_i (°C)	0.4733	0.4851
Rh_i (%)	1.3287	1.3335
$C_{CO2,i}$ (ppm)	40.7634	36.6489
I_l(μmol/(sm^2))	3.5064	3.5201
Bat_{SOC} (%)	39.4408	39.7595
P_{imp} (kW$_e$)	0.2328	0.1562
Q_s (kW$_{th}$)	8.5931	8.6083

reference settings, as depicted in Fig. 10a to 10f. The micro-CHP unit met the greenhouse's heating demand, ensuring the hot water temperature remained within its operating range. Fig. 10e highlights that the battery reached its highest SOC around noon, when solar generation and micro-CHP power generation peaked.

The system's accuracy is quantified in Fig. 10f, which presents Mean Absolute Errors (MAEs) and standard deviations (STDs). Notably, the temperature MAE was 0.49 °C, the relative humidity MAE was 1.33 %, the CO$_2$ concentration MAE was 33.65 ppm, and the lighting intensity MAE was 3.52 μmol/(s·m^2).
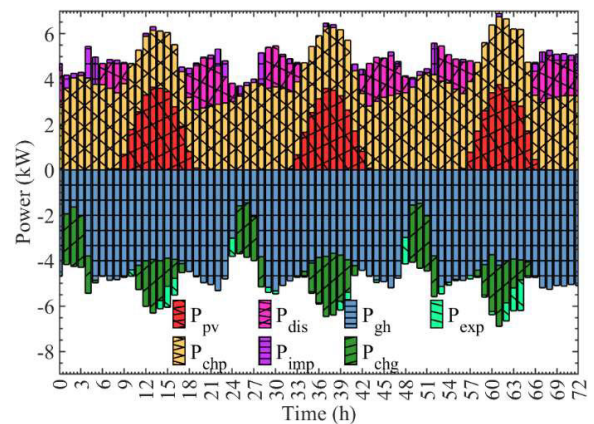
FIGURE 11. Microgrid power balance in case study 2 (case 2*).

Fig. 11 illustrates the microgrid's power balance, showing increased greenhouse load P_{gh} during the period of 4AM to midnight due to higher artificial lighting and CO$_2$ injection operations. From 8AM to 3PM, when solar irradiation was available, the local power production was higher, and it charged the battery.

As illustrative examples, Fig. 12 and Fig. 13 compare the optimal storage state of the battery SOC and the optimal
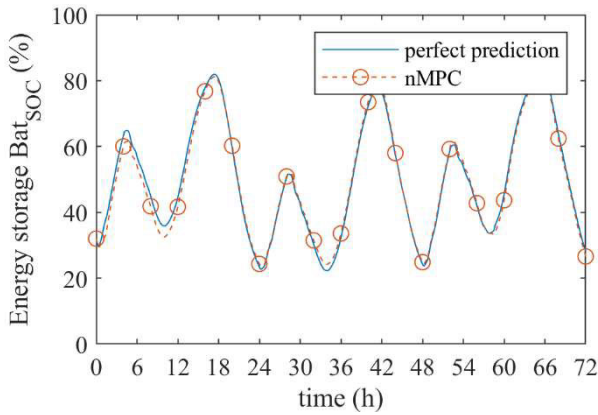
FIGURE 12. Comparison between the optimal battery SOC considering the two approaches.
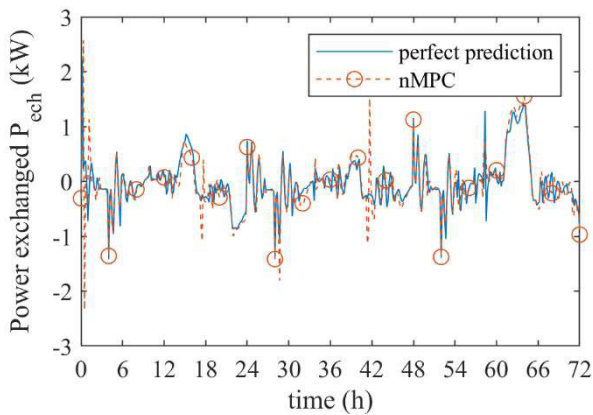

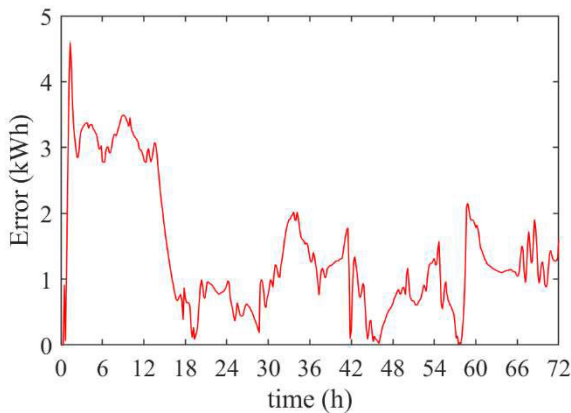**FIGURE 13.** Comparison between the optimal power exchanged with the grid considering two approaches.

FIGURE 14. Energy stored absolute error considering the two approaches.

energy exchanged with the main grid, respectively. These comparisons are made between results obtained using the NMPC algorithm and those assuming perfect predictions. Fig. 14 presents the absolute error in the stored energy of the battery for the two approaches. The analysis of these figures demonstrates that the NMPC optimization effectively

addresses uncertainties, significantly improving the accuracy and quality of the results.

Fig. 15 breaks down the power contributions to the greenhouse load. Local sources provided 83.4% of the total power consumption, with 12.8% supplied by the battery and only 3.8% imported from the grid. These results demonstrate the greenhouse's ability to achieve near-zero energy consumption, emphasizing the effectiveness of the integrated control system.
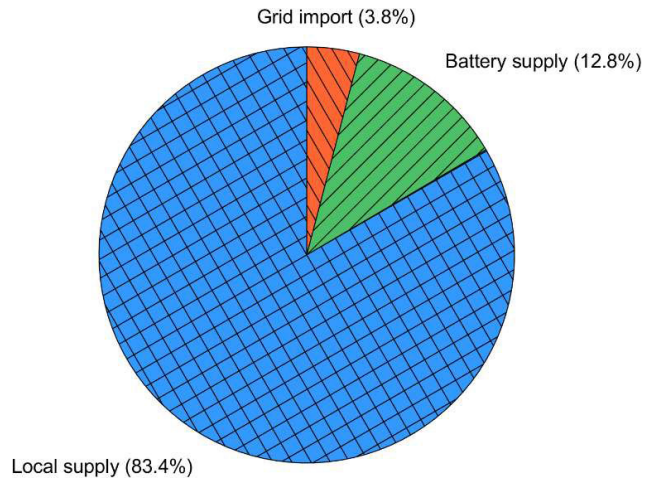

FIGURE 15. Greenhouse load contribution in case study 2 (case 2*).

The solution offers scalability to different types and sizes of greenhouses due to its modular design and adaptability of the control framework. The NMPC and EKF can be reconfigured to account for the unique characteristics and constraints of various greenhouse systems, such as differences in thermal dynamics, energy demands, or microclimate requirements. Additionally, the integration of photovoltaic panels, micro-CHP units, and energy storage systems can be scaled proportionally to match the specific energy and operational needs of each greenhouse, making the solution versatile for diverse agricultural settings.

While the theoretical models and simulations presented offer valuable insights into microclimate control and energy management in smart greenhouses integrated with microgrids, experimental implementation remains essential. Such validation is critical to bridging the gap between theoretical concepts and practical applications, ensuring that the developed models perform reliably under real-world conditions. By conducting experimental studies, unforeseen variables can be addressed, system performance and reliability can be verified, and control strategies can be refined to further optimize energy efficiency and environmental conditions.

IV. CONCLUSION

In this study, we developed a simulator for a smart greenhouse integrated into a microgrid comprising PV panels, micro-CHP unit, and energy storage system. We designed an NMPC combined with an EKF to regulate the main microclimate

parameters, such as temperature, relative humidity, CO_2 concentration, and lighting intensity, and to control the operation of the energy storage system to reduce the power imported from the grid. The simulation results demonstrated that the NMPC effectively controlled the complex system and addressed its nonlinearity. In addition, the EKF mitigated the model noise and measurement errors by correcting the predicted states.

Power contribution analysis revealed that 83.4% of the greenhouse's energy demand was local generation, 12.8% was from the energy storage system, and only a small portion—3.8%— was imported from the main grid. The results indicate that the smart greenhouse integrated with the microgrid successfully achieved near-zero energy consumption.

Since the findings are based on simulations, experimental validation on real greenhouses is essential to confirm their practical feasibility. Additionally, this study assumed that the micro-CHP system would supply heat to the greenhouse during a winter day. To generalize the findings, it is crucial to extend the simulator to account for seasonal variations.

Future work will focus on incorporating seasonal variability, refining NMPC parameter tuning methods, and exploring advanced control strategies, such as reinforcement learning, to further enhance system performance.

ACKNOWLEDGMENT

REFERENCES

[1] R. Ramin Shamshiri, F. Kalantari, K. C. Ting, K. R. Thorp, I. A. Hameed, C. Weltzien, D. Ahmad, and Z. Mojgan Shad, "Advances in greenhouse automation and controlled environment agriculture: A transition to plant factories and urban agriculture," *Int. J. Agricult. Biol. Eng.*, vol. 11, no. 1, pp. 1–22, 2018, doi: 10.25165/j.ijabe.20181101.3210.

[2] Y. Achour, A. Ouammi, and D. Zejli, "Technological progresses in modern sustainable greenhouses cultivation as the path towards precision agriculture," *Renew. Sustain. Energy Rev.*, vol. 147, Sep. 2021, Art. no. 111251, doi: 10.1016/j.rser.2021.111251.

[3] N. Engler and M. Krarti, "Review of energy efficiency in controlled environment agriculture," *Renew. Sustain. Energy Rev.*, vol. 141, May 2021, Art. no. 110786, doi: 10.1016/j.rser.2021.110786.

[4] M. Azaza, C. Tanougast, E. Fabrizio, and A. Mami, "Smart greenhouse fuzzy logic based control system enhanced with wireless data monitoring," *ISA Trans.*, vol. 61, pp. 297–307, Mar. 2016, doi: 10.1016/j.isatra.2015.12.006.

[5] Ravishankar. *Achieving Net Zero Energy Greenhouses By Integrating Semitransparent Organic Solar Cells | Elsevier Enhanced Reader*. Elsevier Inc. Accessed: Oct. 4, 2021. [Online]. Available: https://reader.elsevier.com/reader/sd/pii/S2542435119306336?token=A827AA307E21E079283EB053BB687F162DD08DDE97150D189B7DB1B3D2B39E1F3DE829BsFF94CF70719A21F8782AD947B&originRegion=us-east-1&originCreation=20211005135314

[6] M. Mohsenipour, M. Ebadollahi, H. Rostamzadeh, and M. Amidpour, "Design and evaluation of a solar-based trigeneration system for a nearly zero energy greenhouse in arid region," *J. Cleaner Prod.*, vol. 254, May 2020, Art. no. 119990, doi: 10.1016/j.jclepro.2020.119990.

[7] C. Ceylan and Y. Devrim, "Design and simulation of the PV/PEM fuel cell based hybrid energy system using MATLAB/simulink for greenhouse application," *Int. J. Hydrogen Energy*, vol. 46, no. 42, pp. 22092–22106, Jun. 2021, doi: 10.1016/j.ijhydene.2021.04.034.

[8] N. Yildirim and L. Bilir, "Evaluation of a hybrid system for a nearly zero energy greenhouse," *Energy Convers. Manage.*, vol. 148, pp. 1278–1290, Sep. 2017, doi: 10.1016/j.enconman.2017.06.068.

[9] A. Hussain, I.-S. Choi, Y. H. Im, and H.-M. Kim, "Optimal operation of greenhouses in microgrids perspective," *IEEE Trans. Smart Grid*, vol. 10, no. 3, pp. 3474–3485, May 2019, doi: 10.1109/TSG.2018.2828942.

[10] Y. Achour, A. Ouammi, D. Zejli, and S. Sayadi, "Supervisory model predictive control for optimal operation of a greenhouse indoor environment coping with food-energy-water Nexus," *IEEE Access*, vol. 8, pp. 211562–211575, 2020, doi: 10.1109/ACCESS.2020.3037222.

[11] A. Ouammi, Y. Achour, D. Zejli, and H. Dagdougui, "Supervisory model predictive control for optimal energy management of networked smart greenhouses integrated microgrid," *IEEE Trans. Autom. Sci. Eng.*, vol. 17, no. 1, pp. 117–128, Jan. 2020. [Online]. Available: https://ieeexplore.ieee.org/document/8704275/

[12] A. Ouammi, "Model predictive control for optimal energy management of connected cluster of microgrids with net zero energy multi-greenhouses," *Energy*, vol. 234, Nov. 2021, Art. no. 121274, doi: 10.1016/j.energy.2021.121274.

[13] E. Rezaei, H. Dagdougui, and K. Ojand, "Hierarchical distributed energy management framework for multiple greenhouses considering demand response," *IEEE Trans. Sustain. Energy*, vol. 14, no. 1, pp. 453–464, Jan. 2023, doi: 10.1109/TSTE.2022.3215686.

[14] *Heating, Ventilating and Cooling Greenhouses*, Standard EP406.4, ANSI/ASAE, 2003.

[15] D. Taler and J. Taler, "Simple heat transfer correlations for turbulent tube flow," in *Proc. E3S Web Conf.*, 2017, pp. 1–7, doi: 10.1051/e3sconf/20171302008.

[16] R. A. C. van der Veen and J. Kasmire, "Combined heat and power in Dutch greenhouses: A case study of technology diffusion," *Energy Policy*, vol. 87, pp. 8–16, Dec. 2015, doi: 10.1016/j.enpol.2015.08.040.

[17] M. Olle and A. Viršile, "The effects of light-emitting diode lighting on greenhouse plant growth and quality," *Agricult. Food Sci.*, vol. 22, no. 2, pp. 223–234, Jun. 2013, doi: 10.23986/afsci.7897.

[18] M. W. van Iersel and D. Gianino, "An adaptive control approach for light-emitting diode lights can reduce the energy costs of supplemental lighting in greenhouses," *HortScience*, vol. 52, no. 1, pp. 72–77, Jan. 2017, doi: 10.21273/hortsci11385-16.

[19] P. Pinho, T. Hytönen, M. Rantanen, P. Elomaa, and L. Halonen, "Dynamic control of supplemental lighting intensity in a greenhouse environment," *Lighting Res. Technol.*, vol. 45, no. 3, pp. 295–304, Jun. 2013, doi: 10.1177/1477153512444064.

[20] M. Zhai, T. Yang, Q. Wu, S. Guo, R. Pang, and N. Sun, "Extended Kalman filtering-based nonlinear model predictive control for under-actuated systems with multiple constraints and obstacle avoidance," *IEEE Trans. Cybern.*, vol. 55, no. 1, pp. 369–382, Jan. 2025, doi: 10.1109/TCYB.2024.3488371.

[21] V. A. Bavdekar, A. P. Deshpande, and S. C. Patwardhan, "Identification of process and measurement noise covariance for state and parameter estimation using extended Kalman filter," *J. Process Control*, vol. 21, no. 4, pp. 585–601, Apr. 2011, doi: 10.1016/j.jprocont.2011.01.001.

[22] S. Bolognani, L. Tubiana, and M. Zigliotto, "Extended Kalman filter tuning in sensorless PMSM drives," *IEEE Trans. Ind. Appl.*, vol. 39, no. 6, pp. 1741–1747, Dec. 2003, doi: 10.1109/TIA.2003.818991.

[23] K. L. Shi, T. F. Chan, Y. K. Wong, and S. L. Ho, "Speed estimation of an induction motor drive using an optimized extended Kalman filter," *IEEE Trans. Ind. Electron.*, vol. 49, no. 1, pp. 124–133, Feb. 2002, doi: 10.1109/41.982256.

[24] T. D. Powell, "Automated tuning of an extended Kalman filter using the downhill simplex algorithm," *J. Guid., Control, Dyn.*, vol. 25, no. 5, pp. 901–908, Sep. 2002, doi: 10.2514/2.4983.

[25] Y. Laamari, K. Chafaa, and B. Athamena, "Particle swarm optimization of an extended Kalman filter for speed and rotor flux estimation of an induction motor drive," *Electr. Eng.*, vol. 97, no. 2, pp. 129–138, Jun. 2015, doi: 10.1007/s00202-014-0322-1.

[26] Z. Chen, H. Biggie, N. Ahmed, S. Julier, and C. Heckman, "Kalman filter auto-tuning with consistent and robust Bayesian optimization," *IEEE Trans. Aerosp. Electron. Syst.*, vol. 60, no. 2, pp. 2236–2250, Apr. 2024, doi: 10.1109/TAES.2024.3350587.

[27] R. H. E. Hassanien, M. Li, and F. Yin, "The integration of semi-transparent photovoltaics on greenhouse roof for energy and plant production," *Renew. Energy*, vol. 121, pp. 377–388, Jun. 2018, doi: 10.1016/j.renene.2018.01.044.

TUAN MINH TRAN (Member, IEEE) received the B.S. degree in electrical power engineering from Hanoi University of Technology, Hanoi, Vietnam, in 2003, and the M.S. degree from the Chalmers University of Technology, Gothenburg, Sweden, in 2009. He is currently pursuing the Ph.D. degree in electrical engineering with the Department of Electrical Engineering, École de Technology Supérieure (ETS), Universite du Quebec, Montreal.

He has experiences in power network operation, SCADA system design, and power transformer electrical design.

AHMED OUAMMI received the Ph.D. degree from the Polytechnic School, University of Genoa, Italy, in 2010. He was a Research Fellow at the University of Genoa and worked as an Assistant Professor at National Centre for Scientific and Technical Research (CNRST) and an Associate Professor at Qatar University. He is currently working with the Department of Electrical Engineering, École de Technology Supérieure (ETS), Universite du Quebec, Montreal. His research interests include decision support models, control and optimization of smart grids, and microgrids, with special focus on the implementation of original methods, models and optimal control algorithms with applications to cooperative and interconnected smart systems integrated renewable energy systems.

LOUIS A-DESSAINT (Life Fellow, IEEE) received the B.Ing., M.Sc.A., and Ph.D. degrees in electrical engineering from École Polytechnique de Montréal, QC, Canada, in 1978, 1980, and 1985, respectively.

He is currently working as a Professor with the Department of Electrical Engineering, École de Technology Supérieure (ETS), Universite du Quebec, Montreal. He was the Holder of the Hydro-Quebec TransEnergie Chair on the simulation and control of power systems, from 2001 to 2011, then of the ETS Institutional Chair in the security of power systems, from 2014 to 2017. He is the author of the The MathWorks "SimPowerSystems" (SPS) Blockset. He is an Emeritus Fellow of Canadian Academy of Engineering and a member of Centre d'excellence de l'Universite du Quebec. He was also an Associate Editor of IEEE TRANSACTIONS ON CONTROL SYSTEMS TECHNOLOGY and *IET Journal on Generation, Transmission, and Distribution*.

● ● ●